Extended characterization of alpha particles via laser-induced p-^{11}B fusion reaction in silicon hydrogenated boron-doped thin targets

Milluzzo, G., Belloni, F., Petringa, G., Scuderi, V., Giuffrida, L., Velyhan, A., Verona, C., Picciotto, A., Rosinski, M., Catalano, R., Crivellari, M., Dostal, J., Dudzak, R., Juha, L., Krasa, J., Krupka, M., Krůs, M., Lanzalone, G., Leanza, R., ... Cirrone, G. A. P. (2023). Extended characterization of alpha particles via laser-induced p-^{11}B fusion reaction in silicon hydrogenated boron-doped thin targets. *Journal of Instrumentation*, *18*(07). https://doi.org/10.1088/1748-0221/18/07/c07022

Published in:
Journal of Instrumentation

Document Version:
Publisher's PDF, also known as Version of record

Published by IOP Publishing for Sissa Medialab

Received: *May 29, 2023*
Accepted: *June 26, 2023*
Published: *July 31, 2023*

2nd International Workshop on Proton-Boron Fusion
Catania, Italy
5–8 September 2022

Extended characterization of alpha particles via laser-induced p-^{11}B fusion reaction in silicon hydrogenated boron-doped thin targets

G. Milluzzo,[a,*] **F. Belloni,**[b] **G. Petringa,**[c,d] **V. Scuderi,**[c,d] **L. Giuffrida,**[d,c] **A. Velyhan,**[d] **C. Verona,**[e,f] **A. Picciotto,**[g] **M. Rosinski,**[h] **R. Catalano,**[c] **M. Crivellari,**[g] **J. Dostal,**[i] **R. Dudzak,**[i,j] **L. Juha,**[i] **J. Krasa,**[i] **M. Krupka,**[i,j] **M. Krůs,**[j] **G. Lanzalone,**[c] **R. Leanza,**[c] **C.G. Litrico,**[c] **M. Pfeizer,**[i,j] **F. Schillaci,**[d] **S. Tudisco,**[c] **D. Margarone**[d,c,k] **and G.A.P. Cirrone**[c]

[a] *Sezione di Catania, Istituto Nazionale di Fisica Nucleare, Via Santa Sofia 64, Catania, Italy*
[b] *School of Electrical Engineering and Telecommunications, Faculty of Engineering, UNSW Sydney, 330 Anzac Parade, Kensington NSW 2033, Sydney, Australia*
[c] *Laboratori Nazionali del Sud, Istituto Nazionale di Fisica Nucleare, Via Santa Sofia 62, Catania, Italy*
[d] *ELI Beamlines Facility, The Extreme Light Infrastructure ERIC, Za Radnicí 835, 252 41, Doln. Břežany, Czech Republic*
[e] *Dipartimento di Ingegneria Industriale, Università di Roma 'Tor Vergata', Viale degli Ingegneri, 00133, Rome, Italy*
[f] *Sezione di Roma Tor Vergata, Istituto Nazionale di Fisica Nucleare, Via della Ricerca Scientifica, 00133, Rome, Italy*
[g] *Micro-Nano Facility, Sensors and Devices, Fondazione Bruno Kessler, Via Sommarive, 18 – POVO 38123, Trento, Italy*
[h] *Institute of Plasma Physics and Laser Microfusion, 01-497 Warsaw, Poland*
[i] *Department of Radiation and Chemical Physics, Institute of Physics of the Czech Academy of Sciences, Na Slovance 1999/2 182 00 Prague 8, Prague, Czech Republic*
[j] *Laser Plasma Department, Institute of Plasma Physics of the Czech Academy of Sciences, Za Slovankou 1782/3, Prague, Czech Republic*
[k] *Centre for Plasma Physics, School of Mathematics and Physics, Queen's University Belfast, Belfast BT7 1NN, United Kingdom*

E-mail: giuliana.milluzzo@ct.infn.it

[*] Corresponding author.

https://doi.org/10.1088/1748-0221/18/07/C07022

2023 JINST 18 C07022

Abstract: The nuclear fusion channel of the p-^{11}B reaction producing α particles with multi-MeV kinetic energies was induced by a sub-nanosecond laser pulse focused onto 10 µm thick boron-doped thin targets at intensities of $\sim 10^{16}$ W/cm^2. A full characterization in terms of α particle flux and angular distribution was performed thanks to the simultaneous use of several diagnostics (time-of-flight detectors, nuclear track detectors, and Thomson Parabola spectrometers), which enabled to measure key features of particles produced both in the backward (target front side) and forward (target rear side) directions. Maximum α particle flux and cut-off energy were recorded at small detection angles with respect to the target normal in the backward direction. The maximum kinetic energy shown by the α-particles produced in the nuclear fusion reaction was ascribable to a post-accelerating transient electric field present in the laser-generated plasma, in agreement with our previous preliminary results.

Keywords: Instrumentation and methods for time-of-flight (TOF) spectroscopy; Plasma diagnostics - charged-particle spectroscopy; Solid state detectors; Wake-field acceleration (laser-driven, electron-driven)

2023 JINST 18 C07022

Contents

2023 JINST 18 C07022

1 Introduction

The conventional route to reach nuclear fusion for energy production is mainly founded on the possibility to sustain the nuclear reaction between deuterium and tritium nuclei, yielding one α particle and one neutron. The deuterium-tritium approach has to still face many technological and sustainability challenges, mainly coming from the low availability of the tritium itself and from the radiation damage and huge radioactivity that are induced in the reactor by the high energy neutrons. Considering this, the nuclear reaction where a proton and a boron-11 nucleus fuse yielding three α particles is very attractive. It involves, in fact, only stable isotopes that are abundantly present in nature, and, moreover, no neutrons are produced, at least at the energy of interest for the production of α particles which makes this reaction a very interesting prospective candidate of the new fusion fuel. The interaction of proton beams with ^{11}B nuclei may trigger the activation of many different nuclear reaction channels depending on the system center of mass energy. The so-called "proton-^{11}B fusion channel" remains the only possible inelastic, nonradiative channel at proton beam energies below 2.0 MeV. Experimental investigations report that the p-^{11}B reaction cross-section shows the main resonance peak of 1.4 barns occurring at 675 keV proton energy in the lab [1, 2]. A second resonance is also present at 160 keV with a maximum cross-section of about 100 mbarn. The p-^{11}B reaction mainly proceeds as a sequential decay via the first excited state of ^{8}Be and ends up with three α particles in the final state (p+ ^{11}B $\rightarrow$ ^{8}Be+ α_1 3α) [3]. The primary particle (α_1) and the two secondary ones, generated in the sub-sequent ^{8}Be breakup, shows a continuous energy spectrum, extending down to zero. In the lower energy region, the observed spectrum is a superposition of the α spectrum and the spectrum of strongly scattered protons. For accurate measurements of the cross-section of this reaction, it is essential to separate the α-particle spectrum from that of the scattered protons. On the other side, the possibility to create an *ignited* hydrogen-boron mixture, is much more complicated than the deuterium-tritium case, The proton-boron fusion results, hence, to be impracticable under the classic thermonuclear scheme while the possibility to induce it in

non-equilibrium plasmas generated by high-power lasers interaction with matter, seems to give a very promising perspective producing an impressive enhancement of the reaction rate [4]. In the last 15 years, p-^{11}B fusion has effectively been induced by means of high-power lasers, reporting an impressive progression in the reaction yield [5–10]. Numerous experiments have been carried out using the kJ- class, sub-ns PALS laser with H-enriched borated targets (e.g. hydrogenated B-doped silicon [5, 11, 12])and boron- nitride [8, 9]), and demonstrated the highest α-particle flux to date (above 10^{10}/sr/pulse), despite the relatively low laser intensities (10^{16} W/cm^2). Recently, kJ-class, ps pulses focused to intensities $\sim 10^{19}$ W/cm^2 (LFEX laser) have been used to generate energetic α-particle beams in a geometry known as pitcher-catcher (protons accelerated from a thin CH foil striking a BN target), reporting an α-particle flux around 5×10^9/sr and energies beyond 10 MeV [13]. In this contribution, the results of a recent experimental campaign carried out at the Prague Asterix Laser System irradiating 10 µm thin boron-doped silicon hydrogenated targets will be presented. In particular, a great effort has been addressed into the reconstruction of the full angular distribution of the α particles produced in the reaction in a wide angular (π) range around the target, in both the forward and backward directions.

2 Experimental setup

The experimental run was carried out at the PALS (Prague Asterix Laser System) facility. It is operated in the PALS Research Center, i.e., the joint laboratory of the Institute of Physics (IP-CAS) and the Institute of Plasma Physics (IPP-CAS), both belonging to the Czech Academy of Science. At a fundamental frequency (λ = 1315.2 nm), the iodine photodissociation laser system Asterix provided an average energy of 600 J in a pulse duration of 300 ps (FWHM) on target [14]. The laser beam was tightly focused onto the target; a focal spot diameter of 80 µm makes it possible to reach a laser intensity of $\sim 10^{16}$ W/cm^2 on the target surface. To maximize the laser-plasma absorption, the laser incidence angle was 30°, as shown in figure 1.

The targets used in the experiment were manufactured by the Micro-Nano Facility (MNF) at Fondazione Bruno Kessler in Trento (I) [12], based on a similar scheme already reported in [5]. Targets were made starting from 6-inch standard silicon wafer with a thickness of 300 µm. The target doping was performed by implanting ^{11}B ions on the front side of the wafer with a total fluence of 10^{22} ions/cm^2. at a depth of 200 nm in Silicon (Si). After that, the silicon wafers have been hydrogenated by means of an annealing thermal treatment for 3 hours in an H-environment. Two configurations of such targets were used for the experiment: the hydrogenated 10 µm silicon wafer, doped with the boron atoms, that will be called "SiHB" targets and a 10 µm Si target, lacking of boron atoms and used for the reference shots.

Protons and α particle energy and angular distribution were measured using different detector schemes, such as Silicon Carbide and Diamond detectors in Time of Flight (TOF) configuration [15, 16], CR39 track detectors [17, 18] and Thomson Parabola Spectrometers (TPS). The adopted detector configuration arrangement is reported in figure 1, showing the position of the detectors with respect to the target-normal direction. Diamond (labelled with "D" in figure 1), as well as Silicon Carbide (labelled with "S") detectors with thicknesses in the range of 15–25 µm were used to measure the proton and α particles signals using the Time Of Flight technique [19]. The detectors were placed at different angles and at a sufficient distance from the target to allow the measurement

2023 JINST 18 C07022

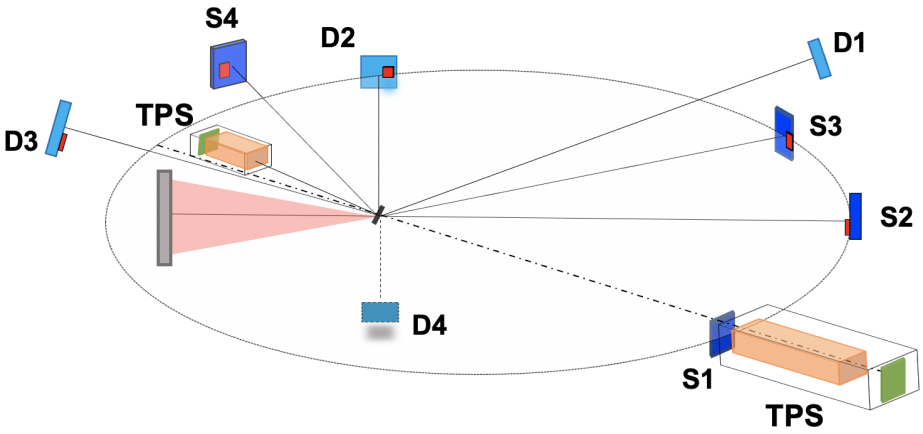

Figure 1. 3-D scheme of the experimental setup employed at PALS during the experimental campaign.

of the particle energy cut-off with a good resolution. The positions of the TOF detectors as respect to the target normal direction (forward direction) are reported in table 1.

Table 1. List of the TOF detectors employed in the experiemnt with the corresponding angular position and distance from the target.

Detector name	Polar angle θ	Flight path [m]	Direction
S1	0°	1.62	Forward
S2	30°	1.51	Forward
S3	60°	1.70	Forward
S4	150°	1.11	Backward
D1	41°	1.43	Forward
D2	120°	0.87	Backward
D3	140°	0.96	Backward
D4	72°	0.83	Forward

Detectors S1, S2, S3 and D2 are placed on the reaction plane (vertical angle $\phi = 0°$) and the total polar angle θ corresponds to the horizontal angle as respect to the target normal, while the detectors S4, D1, D3 and D4 are located out of the plane with a vertical angle $\phi \neq 0$.The total polar angle θ in table 1 has been calculated for these detectors accounting for both the vertical angle and the horizontal angle with respect to the target normal direction.

Aluminium absorbers of different thicknesses (6–25 µm) were placed on the detector surface to stop the low-energy protons and heavy ions. The four diamond-based detectors (D1-D4) were all operating in planar configuration [20]. Approximately 50 µm thick high-quality diamond layer was deposited by Microwave Plasma Enhanced Chemical Vapor Deposition (MWPECVD) on a 4×4×0.5 mm^3 commercial low-cost synthetic diamond substrate at Industrial Engineering Department laboratories of *Tor Vergata* University. Interdigitated chromium electrodes were then realized by photolithography techniques and thermal evaporation of chromium on CVD diamond

2023 JINST 18 C07022

surface. The width and distance between the electrodes are 20 µm [21]. The active area of detectors is about 1 mm^2. The diamond detectors were wire bonded on a dedicated PCB for electrical connections and mounted inside an aluminium shielded holder to reduce electromagnetic pulses noise generated in the high-power laser interaction with the target [22]. Each detector was connected to a fast oscilloscope by low-noise coaxial cables and an integrated bias tee (R = 3.3 M and C = 1 µF) was used to bias the detectors. An external voltage of 60 V was applied between the two metallic contacts. The time resolution is less of 1 ns, as obtained from the detection of single 5.5 MeV α particle emitted by ^{241}Am source [21].

On the other hand, the SiC detectors (S1, S2, S3 and S4 of figure 1) were built growing a 4H-SiC n-type epitaxial layers with a carrier concentration of 2.0 10^{14} cm^{-3} and a thickness of 80 µm on a highly doped n-type (7.0 10^{18} cm^{-3}) substrate. A Schottky junction was realized by a 0.2 µm thick layer of Ni_2Si deposited on the front surface while the ohmic contact, on the back surface, is obtained with a layer of Ni_2Si [23, 24]. The detector is composed of different active areas (chips) ranging from 1 mm × 1 mm up to 2 mm × 2 mm, glued on a brass foil 1 mm thick. A Bias voltage of −400 V was employed for all the SiC detectors corresponding to a depletion layer thickness of ∼ 25 µm.

CR-39 nuclear track detectors were employed to count the particle flux and to discriminate the protons from α particles according to the measurement of the track dimensions. 1 cm^2 CR39 were placed adjacent to each TOF detector aperture as shown in figure 1 (red square), in order to achieve a direct comparison and to obtain complementary information among the two measurements. Aluminium absorbers of different thicknesses were also placed in front of the CR39 detectors to provide different energy cut-off for protons and α particles, thus allowing particle species identification. In particular, CR39 detectors were positioned in a holder equipped with four different aluminium thicknesses to have four different regions in the CR39 detector, each of them with different filtering. Details of the chosen aluminium filters and corresponding minimum energy for protons and α particles to traverse them calculated with the LISE++ software [25] are reported in table 2.

Table 2. Aluminum thickness absorbers used for the four regions in the CR39 with the corresponding minimum energy to traverse for protons and α particles.

Region	Al thickness	Protons	α particles
1	12 µm	0.88 MeV	3.2 MeV
2	16.5 µm	1.09 MeV	4.09 MeV
3	20 µm	1.24 MeV	4.71 MeV
4	25 µm	1.44 MeV	5.52 MeV

Two Thomson Parabola Spectrometer (TPS) were also installed respectively at 0° in the forward direction and at a small angle as respect to the target normal in the backward direction ($\theta < 5°$) (figure 1). A magnetic field is coupled to an electric field in order to disentangle the different ion species accelerated in the laser-target interaction. The particle traces were then detected using a Micro Channel Plates providing real-time information of the particle traces [26]. The TPS were mainly used to check the maximum proton energy along the target normal direction in both backward and forward directions and to identify the ion species and their maximum energies.

2023 JINST 18 C07022

3 Methods

3.1 CR39 analysis

CR-39 nuclear track detectors are commonly used in this field to record the number of particles and identify the different beam components, according to the dimension of detected tracks and their corresponding shape [27]. The CR-39 used for the experiment were previously calibrated with a ^{241}Americium α source in order to establish the correspondence between the track size and the α particle energy and be able to distinguish protons from α particles. A 6.25 M NaOH solution at the fixed temperature of 70 $^{\circ}C$, was used to etch the CR-39. Etching time was varied from 0.5 h up to 2 h. Since the CR39 were irradiated with different aluminium filters (see table 2) the correspondence between the track area in the CR39 and the incident α particle energy (as emitted from the target) was calculated considering the energy loss in each of the filters placed in front of the CR39. Figure 2 shows the incident α particle energy as a function of the detected track area for the four CR39 regions covered by the aluminium absorbers as a result of the calibration. The total etching time was 0.5 h. The track areas span from 5 µm^2 up to 12 µm^2, in the energy range between 4 MeV and 8 MeV.

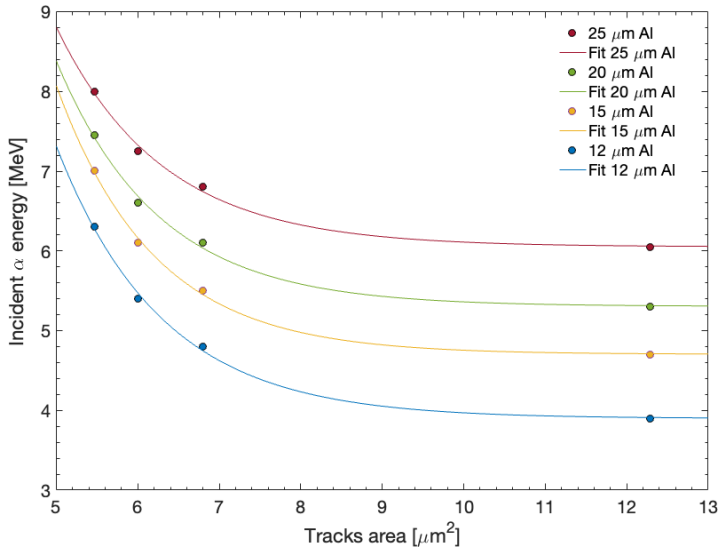

Figure 2. Incident α particle energy and corresponding track area in the CR39 for the 4 regions of the CR39s as resulted from the calibration performed with 0.5 h etching time.

The images of the CR39s positioned at 30° in the forward direction and corresponding to the third region (20 µm aluminium filter) have been acquired for two consecutive shots performed irradiating the SiHB target and the non-borated 10 µm thick Silicon target used as reference, respectively. An etching time of 0.5 h was adopted for the CR39.

The corresponding distribution of the track areas for the two CR39 irradiated is shown in figure 3. In the case of the shot with the SiHB target, where α particles are expected to be produced, the distribution shows the presence of track areas ranging from few µm^2 up to 15 µm^2. The latters are totally absent in the area distribution obtained for the shot performed with the only-Silicon target (yellow histogram in figure 3) where the maximum track area resulted around 5 µm^2. This clearly indicates the presence of a different ion species characterized by bigger track areas in the

2023 JINST 18 C07022

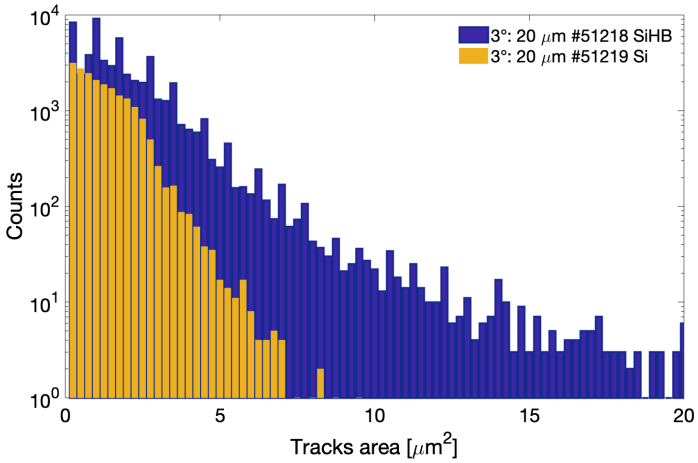

Figure 3. Corresponding track area histograms for the shots under study.

CR39 during the shot with the SiHB target in comparison with the Si target. As expected, in agreement with [27], α particles produce larger track diameters in the CR39 than protons at the same energy/nucleon, at the same etching time. As a matter of fact, also Carbon, Si and Boron ions accelerated from the laser-target interaction could produce a larger track in the CR39 detectors. Nevertheless, the presence of B ions in the nuclear-track detectors is excluded since 20 µm thick Al filter is used, able to stop B ions up to 1.5 MeV/u, well above the typical values reported in the literature at this laser intensities (see [28]). Thus, we can deduce that tracks having an area exceeding about 5 µm^2 are ascribable to α particles only, while the region 0–5 µm^2 can contain both protons and α-particles. Using the alpha particle energy calibration shown in figure 2 we can then convert the track area associated to alpha particles only in incident energy and perform a spectroscopic analysis. In particular, as you can see in the calibration shown in figure 2 related to the region 3 (20 µm Al filter), 5 µm^2 track area in the CR39 corresponds to an incident alpha particle energy of 8.5 MeV, which defines the upper limit in the energy interval where the CR39 analysis is conducted.

3.2 TOF detector analysis

The TOF signal generated in diamond or SiC detector results from the overlapping of the different ion contribution reaching the detector at certain time, depending on their kinetic energy. In the particular case of the p-11B fusion reaction here under investigation, the protons accelerated in the laser-target interaction and the produced alpha particles in the nuclear reaction, reach the detector simultaneously having a similar arrival time [29]. This is due to their energies: α particles produced in p-11B fusion reaction, have an energy ranging from 3 up to 10 MeV and reach the detector placed at a certain distance at the same TOF values of protons having energies ranging from 500 KeV to 3 MeV, being the typical values of proton energies obtained in experiments at PALS. The use of absorbers placed in front of the detectors might help in the discrimination, but only if the proton energy spectrum and cut-off is independently measured. Moreover, the absorber ensures no other ion (carbon, boron etc) contributes to the total signal.

2023 JINST 18 C07022

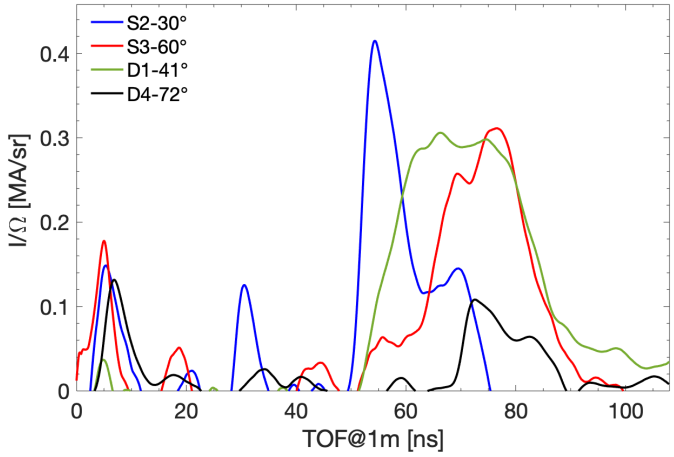

(a)

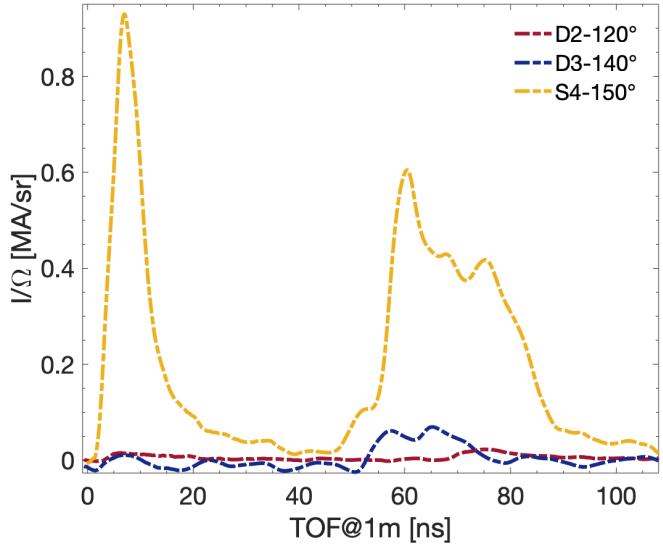

(b)

Figure 4. (a) TOF signals normalized @1 m acquired with the SiC and diamond detectors placed in the forward direction (continuous line) and (b) in the backward direction.

Figure 4 show the TOF signals acquired with the silicon carbide and diamond detectors placed at different angles around the target (forward on the top and backwards on the bottom). The x-axis represents the TOF values normalized at a fixed distance of 1 m, while in the y-axis the particle current per unit of solid angle in steradians is reported, obtained from the signal amplitude (expressed in Volt) as follow:

$$\frac{I}{\Omega} = \frac{V(t)}{R \cdot \Omega} = \frac{V(t) \cdot d^2}{R \cdot \text{Area}_{\text{det}}} \tag{3.1}$$

where R represent the 50 Ω load impedance, Area_{det} is the detector size and d is the flight path. As can be seen from figure 4, where all the signals are normalized at the solid angle of each detector, a very large signal resulting from the sum of both the protons and alpha particles generated, is clearly visible in all the detectors.

2023 JINST 18 C07022

4 Results and discussion

Further measurements of proton energy cut-off and ion species accelerated from plasma were also provided by the TPS placed along the target normal in the forward direction (see figure 1). The shot-to-shot monitoring of proton yield and maximum energy in the case of boron-enriched targets is, indeed, required to verify the conditions to trigger the proton-boron fusion reaction. Figure 5 shows the proton energy spectrum detected during the shot under study (SiHB target) with the Thomson Parabola placed along the target-normal in the forward (black line) and in the backward (red line) direction. In the case of the signal detected in the forward direction, one notes an exponentially decreasing spectrum with a maximum proton energy of 1.7 MeV and a total number of protons per solid angle unit with an energy higher than 0.6 MeV of about 3 $*10^{12}$ p/sr. The lower limit of 0.6 MeV on the detectable proton energy range was due to the Microchannel plate edge.

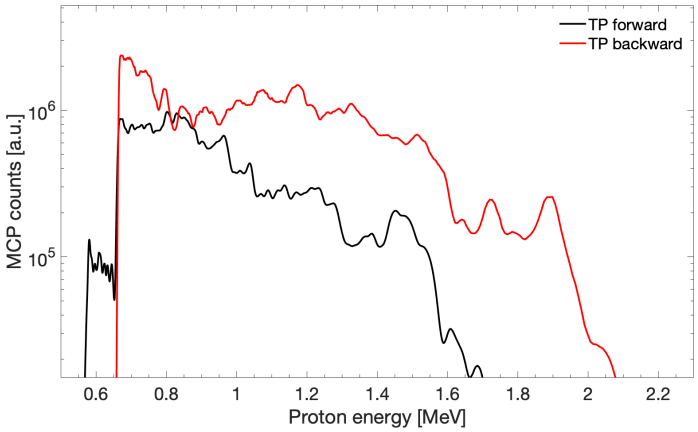

Figure 5. Proton energy distributions detected with the TPs coupled with the Microchannel plate placed along the target-normal in the forward direction (black line) and in the backward direction (red line).

It is worth noting that this is only a part of the protons accelerated by the long laser pulse at the target front side. In fact, protons accelerated forward at the target front surface were either stopped in the target (warm dense matter), or slowed down, thus emerging from the target rear side with a substantially lower energy (<0.6 MeV) that did not allow them to be detected by the TP spectrometer. For what concerns the signal detected in the backward direction (red line in figure 5), a higher energy cutoff exceeding 2 MeV and a slightly higher proton flux can be observed with respect to the signal in the forward direction. The analysis of the different complementary diagnostics, i.e. TOF, CR39 detectors and TP, was carried out with the main goal to allow disentangling the alpha particles produced in the nuclear reaction from the protons accelerated in the laser-plasma. Keeping in mind this goal, the comparison between the CR39 and the TOF detectors placed close to each other was a key aspect of data analysis and interpretation.

According to figure 3, which refers to the CR39 irradiated with 20 µm Al filter, 5 μm^2 has been assumed as the minimum track area in the CR39 that could be attributed to alpha particles. This corresponds to an energy of incident alpha particles of 8.5 MeV. All the tracks having an area in the CR39 exceeding this value, have been considered as alpha particles. This assumption implies that protons produced a track area smaller than 5 μm^2. In such a way, for each CR39 placed at a certain

2023 JINST 18 C07022

angle close to the TOF detectors, it was possible to calculate the percentage of tracks ascribable to alpha particles with respect to the total number of tracks (protons + α particles). The ratio between the track area >5 µm^2 and the total number of tracks has been then used as scale factor to analyse the TOF signals which, as already explained, detect both protons and alpha particles at similar TOF values. This way, it was possible to extract the alpha particle contribution from the TOF signals. Figure 6(a) shows the energy spectrum for the alpha particles obtained using this approach and the technique reported in [30, 31].In particular, the alpha energy spectra obtained at 30° (S2), 41° (D1) and 60° (forward direction) and at 150° (S4) and 140° (D3) (backward direction) are reported.

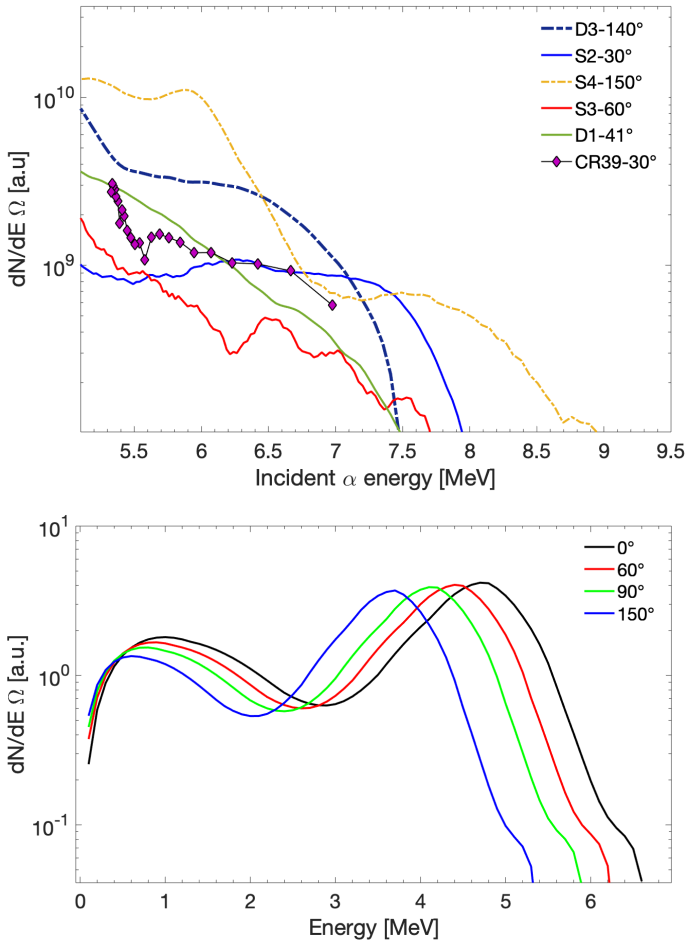

Figure 6. Top: α particle energy distributions measured with the TOF detectors S2, S3, D1 placed at 30°, 41°, 60° (forward direction) and D3, S4 located at 140° 150° (backward direction). The figure also shows the alpha energy spectrum measured with the CR39 placed at 30° and reconstructed from the histogram shown in figure 3 by using the calibration shown in figure 2. Bottom: calculated energy distributions of the emitted α-particles at detection angles of interest (the α_0 peak is not shown). Calculations refer to a 675 keV proton impinging on ^{11}B at rest along the forward direction (θ = 0°).

The lower limit in the energy spectra is given by the 20 µm Al filter that stops alpha particles up to 4.7 MeV (see table 2). The figure also reports the alpha particle energy spectrum retrieved through the spectroscopic analysis of the CR39 placed at 30°, close to the TOF S2. Data have

2023 JINST 18 C07022

been analyzed considering the 20 µm Al foil calibration curve shown in figure 2. Figure 6 (bottom) shows the alpha energy distribution calculated at representative values of the detection angle, θ, for a 675 keV proton impinging along the forward direction ($\theta = 0°$). Calculations are based on a kinematic transformation of an input experimental spectrum from Stave et al. [1]. By the effect of the proton momentum, the spectra show a contraction in both range and amplitude with increasing θ. As a consequence, their endpoint shifts from about 7 MeV at 0° to about 5 MeV in the backward direction (e.g. 150°). On the other hand, the experimental spectra in figure 6(a) demonstrate an endpoint energy approaching 10 MeV in the backward direction (150°). Thus, the experimental value is much higher than the one expected from kinematic calculations. In fact, as preliminarily presented in our previous work [9], the spectral shift towards higher energies can be attributed to the effect of the same quasi-electrostatic potential which accelerates protons backwards. This potential, of the order of 1 MV, also accelerates the alpha particles generated by the forward proton stream and emitted in the backward direction. Their initial energies are then boosted by a few MeV, as observed.

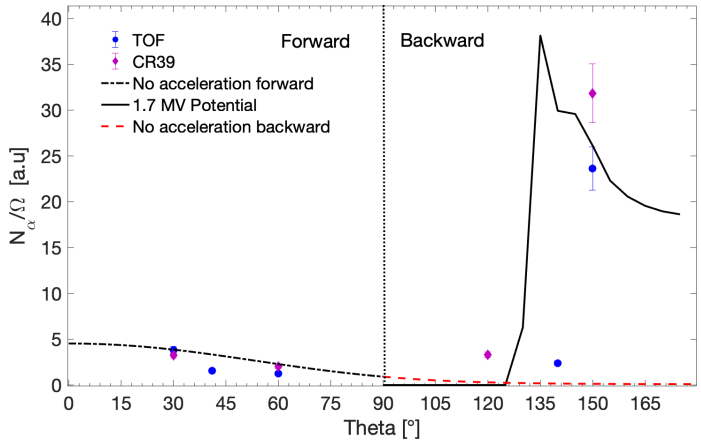

Figure 7. α particles angular distribution in the energy range >5 MeV measured with the TOF detectors (blue points) and with the CR39 detectors (purple points). Angular distributions in the forward and backward semispaces calculated using the same approach of figure 6(b), with (black line) or without (red dashed lines) the presence of a 1.7 MV accelerating electrostatic potential on the front side of the target.

Figure 7 shows the angular distribution based on the TOF detectors placed at 30°, 41°, 60°, 140° and 150°, and for the CR39 detectors placed at 30°, 60°, 120° and 150°. Data points are obtained by integration of the relevant energy spectra (particle energy >5 MeV; see e.g. figure 6a). The yield measured with the TOF detectors is in good agreement with that extracted from the CR39 detectors at the same angular position. Figure 7 also shows the angular distribution calculated for both particles in free-flight (forward semispace) and under the effect of a 1.7 MV potential gap at the laser-target interface (backward semispace). The α particles are assumed to be generated in the target, just outside the gap, by 675 keV protons. The reaction region is supposed to have transverse dimensions much smaller than those of the gap. The gap width is negligible compared to the flight path to the detectors. The electric field in the gap points in the backward direction and is assumed to be constant and uniform, this obviously being a high idealization of its variability in real conditions, as seen in e.g. the backward proton spectrum of figure 4. The calculated angular distribution is obtained by integration of either energy spectra like those in figure 6(b) or their kinematic transformation under

2023 JINST 18 C07022

the effect of the accelerating field. The presence of the filter (20 µm Al) is also considered in the calculation (the filter cutoff is taken as the integration lower bound). It is worth noting that, looking at the calculation (dashed red curve), if no accelerating electric field was present, much less particles would have been detected in the backward semispace compared to the actual experimental yield. Furthermore, the presence of a steep increase in the experimental distribution just after 135° is in reasonable agreement with the theoretical calculations under the assumption of a post-accelerating electric field.

Unfortunately, the lack of detectors at angles between 150° and 180° do not allow to validate the trend of the theoretical curve further. In our simple model,the acceleration gap acts as an electrostatic lens causing a refraction of the particle emission trajectories and the consequent appearance of a limiting angle, l, below which the particle propagation is suppressed in the backward semispace. It is easy to show that upon isotropic emission, $\theta_l$satisfies the relation:

$$tg^2\theta_L = \frac{E_{\max}}{zeV} \tag{4.1}$$

where $E_{\max}$ is the maximum particle emission energy, V is the difference of potential across the electrostatic gap, and ze is the particle electric charge ($z = 2$ for alpha particles). Conversely, eq. (4.1) can be used to estimate V once θ_l is measured. In our case, with θ_l between 120° and 135°, and $E_{\max}$ ~6 MeV (figure 6b, 90° curve), we find V ranging between 1 and 3 MV (note the extreme sensitivity of V to the uncertainty on θ_l). Values below 2 MV are in line with the effective magnitude of the accelerating potential one can infer from the proton spectrum of figure 5 (red curve).

5 Conclusion and discussion

The alpha particle energy and angular emission from laser-induced p-^{11}B fusion reactions were measured on a very wide solid angle for the first time. This allowed to retrieve key information on the alpha particle dynamics in the plasma generated by a long (sub-ns) laser pulse delivering kJ-level energy on target. The approach used in this work (covering the entire solid angle around the target with a large number of active and passive detectors) allowed to extend our previous experimental studies [5, 8, 9], where the measurement of the α particle yield was limited to a few angles in the backward direction (target front side).This allowed to confirm the presence of an electric potential at the target front side that was responsible for a post-acceleration of the alpha-particles generated via p-^{11}B fusion reactions. In fact, this quasi-electrostatic field is the same that causes acceleration of plasma protons at relatively high energies (1.5–2 MeV) in the backward direction. Thus, under the assumption of an effective 1.5–2 MV post-accelerating potential, the alpha particles would gain an additional energy of 3–4 MeV, which justifies the enhanced spectral endpoints measured in the backward direction (up to 9 MeV). The presence of a post-accelerating field was hypothesized in [9] in agreement with the theory reported in [32–34] is confirmed by this study, thus paving the way towards new schemes to enhance the output energy of nuclear reaction products in a laser-plasma environment. The datasets generated during and/or analysed during the current study are available from the corresponding author upon reasonable request. The authors declare no conflicts of interest.

2023 JINST 18 C07022

Acknowledgments

The authors wish to thank the Interdisciplinary Committee of the Istituto Italiano di Fisica Nucleare (INFN). Authors have to thank the Czech Ministry of Education, Sports and Youth (CMEYS) for financial support to make possible the operation of the PALS facility (grant nr. LM2018114, project No.LQ1606). The work has been also supported by the projects Advanced Research Using High Intensity Laser Produced Photons and Particles (CZ.02.1.01/0.0/0.0/16_019/0000789), by the Royal Society International Exchanges project (No. IES/R2/203175). This article/publication is based upon work from COST Action PROBONO, CA21128, supported by COST (European Cooperation in Science and Technology. Thanks go also to the technical staff of the PALS facility, namely to Jiri Kovar, Jiri Skala, Jakub Mares, Pavel Prchal, Leos Vedral, Dalibor Jesatko,Zdenek Vancura, and Eduard Horvath, for their technical support of the facility operation and the experiment itself.

References

[1] S. Stave et al., *Understanding the* $^{11}B(p,\alpha)\alpha\alpha$ *reaction at the* 0.675 *MeV resonance*, *Phys. Lett. B* **696** (2011) 26.

[2] M.H. Sikora and H.R. Weller, *A new evaluation of the* $^{11}B(p,\alpha)\alpha\alpha$ *reaction rates*, *J. Fusion Energy* **35** (2016) 538.

[3] H.W. Becker et al., *Low-Energy Cross Sections for* $^{11}B(p,3a)$, *Z. Phys. A* **327** (1987) 341.

[4] D. Margarone et al., *In-Target Proton–Boron Nuclear Fusion Using a PW-Class Laser*, *Appl. Sci.* **12** (2022) 1444.

[5] A. Picciotto et al., *Boron-Proton Nuclear-Fusion Enhancement Induced in Boron-Doped Silicon Targets by Low-Contrast Pulsed Laser*, *Phys. Rev. X* **4** (2014) 031030.

[6] V.S. Belyaev et al., *Observation of neutronless fusion reactions in picosecond laser plasmas*, *Phys. Rev. E* **72** (2005) 026406.

[7] D. Margarone et al., *Advanced scheme for high-yield laser driven nuclear reactions*, *Plasma Phys. Control. Fusion* **57** (2015) 014030.

[8] C. Labaune et al., *Laser-initiated primary and secondary nuclear reactions in Boron-Nitride*, *Sci. Rep.* **6** (2016) 21202.

[9] L. Giuffrida et al., *High-current stream of energetic* α *particles from laser-driven proton-boron fusion*, *Phys. Rev. E* **101** (2020) 013204.

[10] J. Bonvalet et al., *Energetic* α*-particle sources produced through proton-boron reactions by high-energy high-intensity laser beams*, *Phys. Rev. E* **103** (2021) 053202.

[11] A. Picciotto et al., *Laser-driven acceleration of protons from hydrogenated annealed silicon targets*, *Europhys. Lett.* **92** (2010) 34008.

[12] A. Picciotto et al., *Microfabrication of Silicon Hydrogenated Thin Targets for Multi-MeV Laser-Driven Proton Acceleration*, *Appl. Phys. Express* **4** (2011) 126401.

[13] D. Margarone et al., *Generation of* α*-Particle Beams With a Multi-kJ, Peta-Watt Class Laser System*, *Front. Phys.* **8** (2020) 343.

[14] K. Jungwirth et al., *The prague asterix laser system*, *Phys. Plasmas* **8** (2001) 2495.

2023 JINST 18 C07022

[15] D. Margarone et al., *Full characterization of laser-accelerated ion beams using Faraday cup, silicon carbide, and single-crystal diamond detectors*, *J. Appl. Phys.* **109** (2011) 103302.

[16] G. Milluzzo et al., *TOF technique for laser-driven proton beam diagnostics for the ELIMED beamline*, 2017 *JINST* **12** C03044.

[17] R.L. Fleischer, P.B. Price and R.M. Walker, *Ion explosion spike mechanism for formation of charged-particle tracks in solids*, *J. Appl. Phys.* **36** (1965) 3645.

[18] B. Cartwright, E. Shirk and P. Price, *A nuclear-track-recording polymer of unique sensitivity and resolution*, *Nucl. Instrum. Meth.* **153** (1978) 457.

[19] G. Milluzzo et al., *Laser-accelerated ion beam diagnostics with TOF detectors for the ELIMED beam line*, 2017 *JINST* **12** C02025.

[20] M. Marinelli et al., *Analysis of laser-generated plasma ionizing radiation by synthetic single crystal diamond detectors*, *Appl. Surf. Sci.* **272** (2013) 104.

[21] C. Verona et al., *Comparison of single crystal diamond TOF detectors in planar and transverse configuration*, 2020 *JINST* **15** C09066.

[22] M. Salvadori et al., *Accurate spectra for high energy ions by advanced time-of-flight diamond-detector schemes in experiments with high energy and intensity lasers*, *Sci. Rep.* **11** (2021) 3071 [arXiv:2003.01442].

[23] F. Nava, G. Bertuccio, A. Cavallini and E. Vittone, *Silicon carbide and its use as a radiation detector material*, *Meas. Sci. Technol.* **19** (2008) 102001.

[24] G. Raciti, M.D. Napoli, F. Giacoppo, E. Rapisarda and C. Sfienti, *Detection properties and radiation damage effects in SiC diodes irradiated with light ions*, *Nucl. Phys. A* **834** (2010) 784c.

[25] http://lise.nscl.msu.edu/lise.html.

[26] F. Grepl et al., *Distortion of thomson parabolic-like proton patterns due to electromagnetic interference*, *Appl. Sci.* **11** (2021) 4484.

[27] C. Baccou et al., *CR-39 track detector calibration for H, He, and C ions from 0.1–0.5 MeV up to 5 MeV for laser-induced nuclear fusion product identification*, *Rev. Sci. Instrum.* **86** (2015) 083307.

[28] S.J. Gitomer et al., *Fast ions and hot electrons in the laser-plasma interaction*, *Phys. Fluids* **29** (1986) 2679.

[29] F. Consoli et al., *Diagnostic Methodologies of Laser-Initiated* $^{11}B(p,\alpha)2\alpha$ *Fusion Reactions*, *Front. Phys.* **8** (2020) 561492.

[30] G. Milluzzo et al., *A new energy spectrum reconstruction method for Time-Of-Flight diagnostics of high-energy laser-driven protons*, *Rev. Sci. Instrum.* **90** (2019) 083303 [arXiv:1812.01357].

[31] V. Scuderi et al., *TOF diagnosis of laser accelerated, high-energy protons*, *Nucl. Instrum. Meth. A* **978** (2020) 164364.

[32] H. Hora, P. Lalousis and S. Eliezer, *Analysis of the inverted double layers produced by nonlinear forces in a laser-produced plasma*, *Phys. Rev. Lett.* **53** (1984) 1650.

[33] S. Eliezer and H. Hora, *Double layers in laser-produced plasmas*, *Phys. Rept.* **172** (1989) 339.

[34] S. Eliezer et al., *Double layer acceleration by laser radiation*, *Laser Part. Beams* **32** (2014) 211.

2023 JINST 18 C07022